Building and Environment, Vol. 24, No. 1, pp. 51–64, 1989.
Printed in Great Britain.

0360–1323/8
© 1989 Pergam

Three-Dimensional Numerical Simulation of Turbulent Flow Around Buildings using the k–ε Turbulence Model

SHUZO MURAKAMI*
AKASHI MOCHIDA*

Three-dimensional numerical simulations of air flow around a cubic model and building complex using the k–ε two equation turbulence model are presented in this paper. Several cases of numerical simulation of airflow around a cubic model are carried out to estimate the influences of a mesh dividing system and boundary conditions on simulated results. The accuracy of these simulations is examined by comparing the predicted results with wind tunnel experiments conducted by the authors. It is confirmed that numerical simulations by means of the k–ε model reproduce the velocity and pressure fields well when using fine mesh resolution around the model. In the latter half of this paper, the numerical method is applied in order to predict the flow field around a building complex under construction at present. The applicability of the numerical method in practical situations is demonstrated.

NOMENCLATURE†

- C_p pressure coefficient, $C_p = (P-P_0)/(\frac{1}{2}\rho U_b^2)$
- $\tilde{e}_h$ solution error estimated by calculation of mesh size h
- h_1 minimum mesh interval adjacent to solid wall (*cf.* Fig. 4)
- H_b height of cubic model
- k turbulence kinetic energy, $k = \frac{1}{2}\overline{u_i' u_i'}$
- l length scale of turbulence
- P pressure
- P_0 reference static pressure
- Re Reynolds number
- u_* friction velocity
- U_b velocity at inflow boundary of computational domain at height of H_b
- U_i $i = 1$ (streamwise, x), 2 (spanwise, y), 3 (vertical, z), three components of velocity vector in x_i direction
- U, V, W X, Y, Z components of velocity vector
- ε turbulence dissipation rate,

$$\varepsilon = C_D k^{3/2}/l = 2\nu \overline{\frac{\partial u_i'}{\partial x_j}\frac{\partial u_i'}{\partial x_j}}$$

- $\tilde{\tau}_h$ truncation error of mesh size h
- ν, ν_t kinematic viscosity, eddy viscosity, $\nu_t = k^{1/2} l = C_D k^2/\varepsilon$

1. INTRODUCTION

THE AIRFLOW around building placed within a surface boundary layer is fully turbulent and very complicated. It is composed of separations at windward corners of the building, the circulations behind it, etc. A 3-D numerical method for turbulent flow should therefore be established from the viewpoint of engineering application in the field of building aerodynamics. A wide variety of numerical approaches, made possible by the recent, rapid advance of computer technology, have been developed in order to predict the turbulent flow field around a building [1–10]. These approaches use different types of flow modelling, i.e. large eddy simulation [6, 9] and direct simulation (with third order up-wind scheme) [8] for predicting unsteady flow fields, and simulations based on Reynolds-averaged Navier–Stokes equations represented by the k–ε two equation turbulence model for predicting steady flow fields. Among these approaches, the k–ε turbulence model, which has been widely applied and examined in many flow phenomena, is the most promising method for engineering applications concerning the problem of wind engineering at present.

Numerical studies of airflow around buildings by means of the k–ε turbulence model have been carried out by many authors. However, only a few studies have been conducted which examine the accuracy of the results from the k–ε model, except for the works by Paterson *et al.* [3] and Baetke *et al.* [7]. There have also been very few studies in which the distribution of turbulent energy (k) has been examined, although the information of k is indispensable for understanding the properties of a flow field. This lack of research is due to the fact that the experimental data currently available for use do not give a detailed distribution for k near the building. In this study, the authors conducted precise measurements of the turbulent flow around the model of a building, including the measurement of k, in order to compare the numerical results with the experimental results.

The Reynolds numbers of the flow fields treated in this study are generally high, due to the large length scale imposed, which makes it very difficult to set the mesh interval near solid walls fine enough to resolve the viscous sub-layer. Therefore, a systematic analysis should be made in order to estimate the influence of the mesh resolution near the solid wall and the treatments of the viscous sub-layer on the predicted flow field. In the first half of this paper, six cases of numerical simulations by

* Institute of Industrial Science, University of Tokyo, Japan.
† All properties are non-dimensionalized by H_b and U_b.

means of the k–ε turbulence model were conducted, using different types of mesh dividings, and different treatments of the boundary layer along the solid wall. A cubic-shaped model was used as the model of a building in these simulations. The accuracy of the simulations was examined by comparing the numerical results with the results of wind tunnel experiments conducted by the authors. In the latter half of the paper, the numerical method is applied to the prediction of the flow field around a building complex under construction at present.

2. NUMERICAL SIMULATION OF AIRFLOW AROUND A CUBIC MODEL

2.1. *Outline of the numerical simulation*

2.1.1. *Cases for numerical simulation.* Specifications of the computed cases are shown in Table 1. Six cases of numerical simulation are carried out to estimate the influence of the following factors on the numerical results: (i) mesh dividings near the building model (Phase 1); (ii) boundary conditions for rigid walls (Phase 2). Here, all variables are made non-dimensional by H_b and U_b. H_b is the height of the cubic model and U_b is the approaching wind velocity at model height H_b.

2.1.2. *Model equations and numerical method.* The governing equations for the k–ε two equation turbulence model are shown in Table 2. The values of numerical constants are the same as those in the original paper by Launder and Spalding [11]. A staggered grid system is adopted here. The definition points of variables are the same as those in the usual MAC method (velocity components at the centre of the cell surface, and scalar quantities in the centre of the cell) [12]. The second order centred difference scheme is adopted for all spatial derivatives except the convective terms of transport equations of scalar quantities (k and ε). For the convective terms of scalar quantities, a first order up-wind scheme is used in Cases 2–6. In Case 1, a second order up-wind scheme (QUICK scheme [13]) is used for the term in order to estimate the error distribution with a second order accuracy. The governing equations are solved in a time dependent system in which the Adams–Bashforth scheme is used. Numerical integrations are conducted following the ABMAC method (simultaneous iteration method for pressure and velocities) [14].

2.1.3. *Mesh dividings.* The mesh dividings used in this study are shown in Fig. 1 and Table 3. Mesh 1 is a uniform spacing mesh, the computational domain of which has a downstream length of $10H_b$, lateral width of $3.5H_b$, and a vertical height of $4H_b$. The mesh interval is $H_b/6$ in Mesh 1. The distribution of errors arising from the finite difference method in the solution with this mesh is estimated in Case 1 (Phase 1, *cf.* Table 1). In Case 1, the symmetry of the flow field in the y-direction is assumed and one half of the flow field is calculated.

Table 1. Specifications of the computed cases for cubic model

Phase	Case no.	Mesh dividing systems*	Boundary conditions at solid walls†	Remarks
1	Case 1	Mesh 1	Type 1	Mesh resolution is changed
	Case 2	Mesh 2	Type 1	
	Case 3	Mesh 3	Type 1	
	Case 4	Mesh 4	Type 1	
2	Case 5	Mesh 2	Type 1′	Boundary condition at solid wall is changed
	Case 6	Mesh 4	Type 2	

* *cf.* Fig. 1 and Table 3.

† Type 1: Equations (6) and (7); Type 1′: Equations (6) and (7), l is set equal to a quarter value of that in Type 1; Type 2: Equations (8) and (9).

Table 2. Model equations (two equation of k–ε type)

$$\frac{\partial U_i}{\partial x_i} = 0 \qquad \text{(1) Continuity equation.}$$

$$\frac{\partial U_i}{\partial t} + \frac{\partial U_i U_j}{\partial x_j} = -\frac{\partial}{\partial x_i}\left(\frac{P}{\rho} + \frac{2}{3}k\right) + \frac{\partial}{\partial x_i}\left\{\nu_t\left(\frac{\partial U_i}{\partial x_j} + \frac{\partial U_j}{\partial x_i}\right)\right\} \qquad \text{(2) Momentum equation.}$$

$$\frac{\partial k}{\partial t} + \frac{\partial k U_i}{\partial x_j} = \frac{\partial}{\partial x_j}\left(\frac{\nu_t}{\sigma_1}\frac{\partial k}{\partial x_j}\right) + \nu_t S - \varepsilon \qquad \text{(3) Transport equation for } k.$$

$$\frac{\partial \varepsilon}{\partial t} + \frac{\partial \varepsilon U_i}{\partial x_j} = \frac{\partial}{\partial x_j}\left(\frac{\nu_t}{\sigma_2}\frac{\partial \varepsilon}{\partial x_j}\right) + C_1\frac{\varepsilon}{k}\nu_t S - C_1\frac{\varepsilon^2}{k} \qquad \text{(4) Transport equation for } \varepsilon.$$

$$\nu_t = k^{1/2} l = C_D\frac{k^2}{\varepsilon} \qquad \text{(5) Equation for deciding } \nu_t.$$

Here: $S = \left(\frac{\partial U_i}{\partial x_j} + \frac{\partial U_j}{\partial x_i}\right)\frac{\partial U_i}{\partial x_j}$, $\sigma_1 = 1.0$, $\sigma_2 = 1.3$, $C_D = 0.09$, $C_1 = 1.44$, $C_2 = 1.92$.

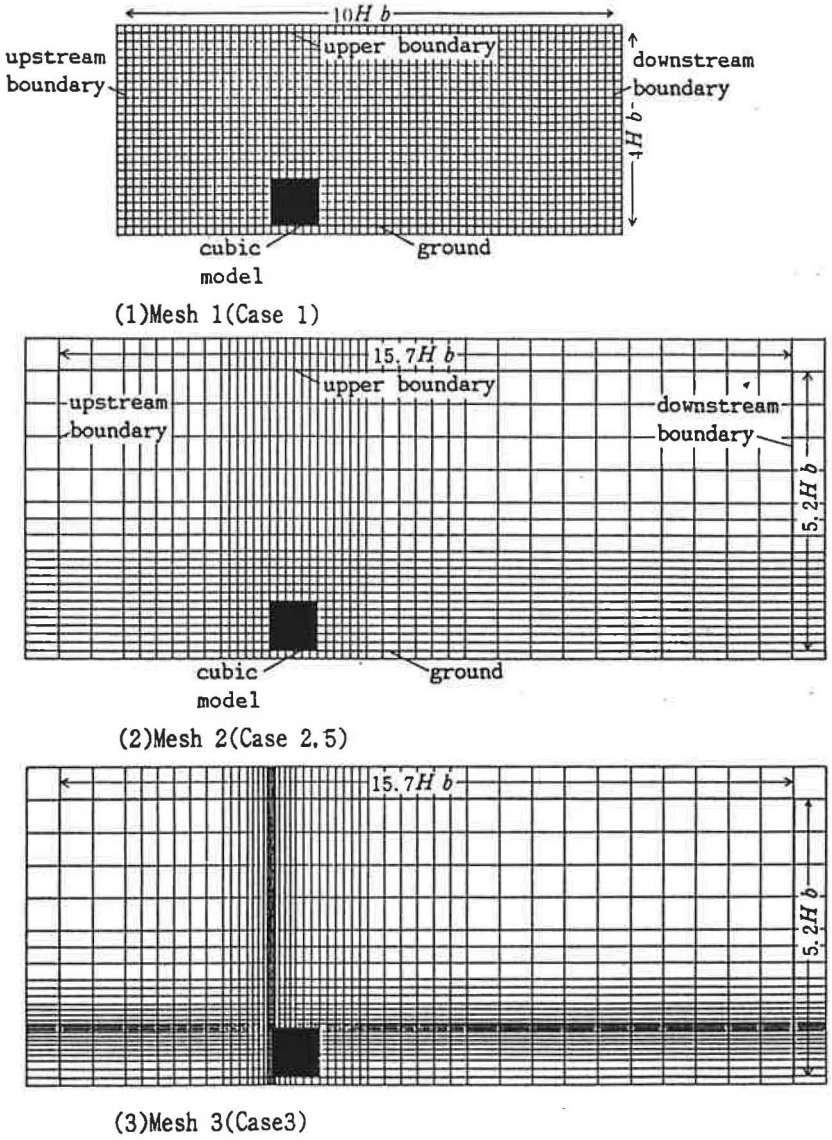

Fig. 1. Mesh dividings (vertical plane).

Meshes 2–4 are mesh systems of non-uniform spacing. All of them have the same computation domain of $15.7H_b$ (downstream length), $9.7H_b$ (lateral width), and $5.2H_b$ (vertical height). The results of numerical simulations using these meshes are compared with the results of the wind tunnel experiments. The mesh interval, h_1, around the model is $H_b/6$ with Mesh 2. With Mesh 3, the mesh interval h_1 around the windward corner is $H_b/24$ and the value around the leeward corner is $H_b/6$. With Mesh 4, mesh intervals h_1 near the model are $H_b/24$ on both the windward and the leeward sides.

2.1.4. *Boundary conditions.*

(1) Upstream boundary. Experimental values measured in a wind tunnel are given for streamwise velocity

Table 3. Specification of mesh dividings

Mesh 1 (Fig. 1(1))	$62(x)\times 23(y)\times 26(z) = 37{,}076$ $(10.0H_b(x)\times 3.5H_b(y)\times 4.0H_b(z))$	Uniform spacing mesh, $h_1 = H_b/6$.
Mesh 2 (Fig. 1(2))	$45(x)\times 37(y)\times 21(z) = 34{,}965$ $(15.7H_b(x)\times 9.7H_b(y)\times 5.2H_b(z))$	Non-uniform spacing mesh, $h_1 = H_b/6$.
Mesh 3 (Fig. 1(3))	$50(x)\times 49(y)\times 28(z) = 68{,}600$ $(15.7H_b(x)\times 9.7H_b(y)\times 5.2H_b(z))$	Non-uniform spacing mesh, $h_1 = H_b/24$. The mesh distribution is concentrated near the windward corner.
Mesh 4	$50(x)\times 49(y)\times 28(z) = 68{,}600$ $(15.0H_b(x)\times 9.7H_b(y)\times 5.2H_b(z))$	Non-uniform spacing mesh, $h_1 = H_b/24$. The mesh distribution is concentrated near the windward corner and the leeward corner.

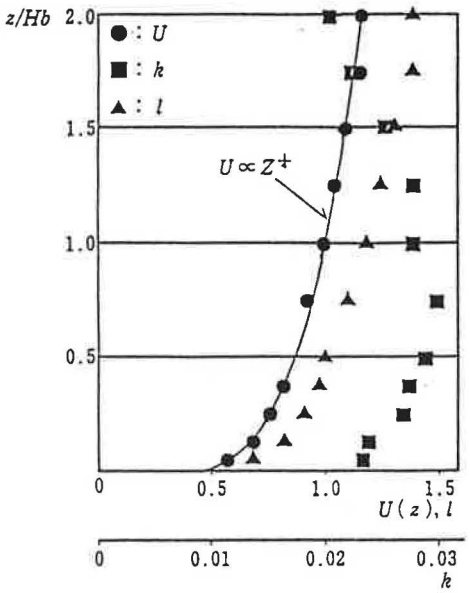

Fig. 2. Inflow boundary conditions (non-dimensionalized by U_b and H_b) measured in wind tunnel.

($U(z)$) and turbulent kinetic energy ($k(z)$) as shown in Fig. 2. Other velocity components $V(z)$ and $W(z)$ are set to zero. The vertical profile of $\varepsilon(z)$ is set to obey the next relation

$$\varepsilon(z) = C_D k(z)^{3/2}/l(z). \tag{6}$$

Here, the vertical profile of length scale ($l(z)$) is defined using vertical profiles of integral scale measured in a wind tunnel, namely:

$$l(z) = C_D^{1/4} U(z) \int R\tau \, d\tau. \tag{7}$$

(2) Upper and side faces of computational domain. The normal gradients of the tangential velocity components (U_i), k and ε, are set to zero. Pressures outside the upper and side faces of the computational domain are set to zero. No boundary conditions are required for the normal velocity component; it is estimated from the momentum equation. Figure 3 illustrates the staggered grids near the upper face. In this condition, the normal velocity need not be set to zero (in Fig. 3, $w_2 \neq 0$).

(3) Downstream boundary. Pressures outside the boundary are assumed to be zero. Normal gradients of tangential velocity, k and ε are set to zero.

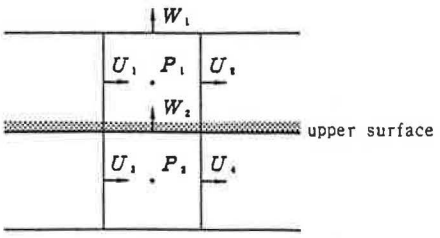

Fig. 3. Staggered grid near the upper surface of the computational domain.

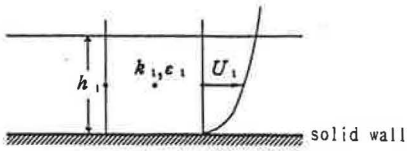

Fig. 4. Staggered grid adjacent to the solid wall. (k_1' is defined at the same point as U_1).

(4) Wall boundary. Figure 4 illustrates the staggered grid adjacent to the wall. It is difficult to set the mesh interval adjacent to the wall fine enough to resolve the viscous sub-layer in the simulations of high Reynolds number flow, such as airflow around the buildings. In this type of flow simulation, it has been proved that the no-slip condition does not provide good results. Some types of artificial boundary conditions should be introduced to compensate for the effect of the viscous sub-layer. In this study, two types of artificial conditions are employed and compared.

In Type 1 (Cases 1–5, *cf.* Table 1), the profiles of the tangential velocity components are assumed to obey a power law expressed as:

$$U(z)/U_1 = (z/\tfrac{1}{2}h_1)^{1/4}. \tag{8}$$

The normal gradient of k is zero; ε at the first grid point is given by:

$$\varepsilon_1 = C_D k_1^{3/2}/l, \quad l = C_D^{1/4} \tfrac{1}{2}\kappa h_1. \tag{9}$$

In Type 2, the generalized log law described in detail by Launder and Spalding [15] is employed. Here, the shear stress at the wall $(\tau/\rho)_w$ is supposed to obey the relation:

$$\frac{U_1}{(\tau/\rho)_w}(C_D^{1/2}k_1')^{1/2} = \frac{1}{k}\ln\left\{E\cdot\frac{\frac{1}{2}h_1(C_D^{1/2}k_1')^{1/2}}{\nu}\right\}, \tag{10}$$

where $E = 9.0$ and k_1' is the value of k interpolated at the definition point of U_1. The value of ε averaged over the control volume adjacent to the wall is assigned using the relation:

$$\varepsilon_1 = \frac{C_D^{3/4}k_1^{3/2}}{\kappa h_1}\ln\left\{\frac{E\cdot h_1(C_D^{1/2}k_1)^{1/2}}{\nu}\right\}. \tag{11}$$

2.2. *Outline of wind tunnel experiments*

A cubic-shaped model, 200 mm in height, is used as the model of a building. The Reynolds number of the experiment based on U_b and H_b is about 7×10^4. The wind velocity is measured by a tandem-type, hot wire anemometer which can discern each component of an instantaneous velocity vector. The mean surface pressure is measured by a BARATRON transducer (Type 210).

2.3. *Comparison between numerical simulation and experimental results*

2.3.1. *Influence of mesh resolution (simulation of Phase* 1). There are two points that should be considered regarding mesh resolution near the windward corners: (a) the computational domain should be large enough so that boundary conditions on the upper and side faces have

little influence on the predicted flow field around the model; (b) the mesh size should be small enough to resolve important flow regimes such as separation zones. It is difficult to meet these requirements thoroughly due to limitation of computer resources. Thus, it is necessary to carefully design how finely each area should be divided in order to obtain simulation results with small errors.

(1) Distributions of truncation error $\tilde{\tau}_h$ and solution error $\tilde{e}_h$ around the model. In this paper, the distributions of two types of errors, namely solution errors and truncation errors, are estimated by Richardson extrapolation. The details of the error estimation method are given by Caruso and Ferziger [16].

The solution error is the residual between the exact solution and the solution of the finite difference method. In the method used here, we assume that the solution error can be expressed as a Taylor series. If the finite difference scheme has a second order accuracy, the solution error (e_h) of mesh size (h) can be estimated with a small amount of algebra as follows [16]:

$$\tilde{e}_h = (U_h - U_{2h})/3, \tag{12}$$

where U_h is the solution of mesh size h, and U_{2h} is the solution of mesh size $2h$.

Truncation errors arise in finite difference approximation. In operator form, the differential equation to be solved is expressed as below:

$$L[U_{EX}] = f, \tag{13}$$

where U_{EX} is the exact solution and L is the spatial differential operator. The truncation error (τ_h) is defined as the residual obtained by substituting the exact solution of the differential equation U_{EX} into the finite difference equation, i.e.

$$\begin{aligned}\tau_h &= L_h[U_{EX}] - L[U_{EX}] \\ &= L_h[U_{EX}] - f,\end{aligned} \tag{14}$$

where L_h is the spatial difference operator. Here the exact solution U_{EX} is estimated by:

$$\tilde{U}_{EX} = U_h + \tilde{e}_h. \tag{15}$$

$\tilde{U}_{EX}$ is used in place of the exact solution U_{EX} in Equation (14) to estimate the truncation error:

$$\tilde{\tau}_h = L_h[\tilde{U}_{EX}] - f. \tag{16}$$

If a very accurate solution is obtained with mesh size h, the solution error (e_h) is estimated to be very small at all mesh points by Equation (12). Truncation errors are regarded as the source of solution errors and are supposed to be concentrated at the region where large gradients of variables exist. If we can decrease truncation error in this region, the solution error will become small in the whole computational domain.

Distributions of errors with Mesh 1 ($h = H_b/6$) are illustrated in Fig. 5. Figure 5(1) shows the distribution of truncation error, $\tilde{\tau}_h$. These errors centre in the region in front of the model. The distribution of solution error ($\tilde{e}_h$) is given in Fig. 5(2). High values of truncation error arising around the windward corner are convected and diffused: as a result, rather high values for solution errors are distributed in the whole flow field around the model.

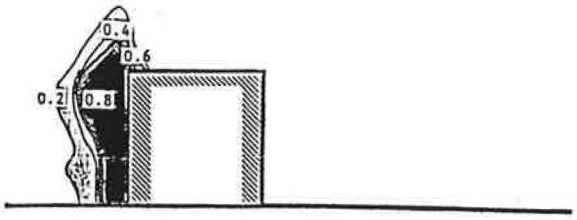

(1)truncation error $\tilde{\tau}_h$

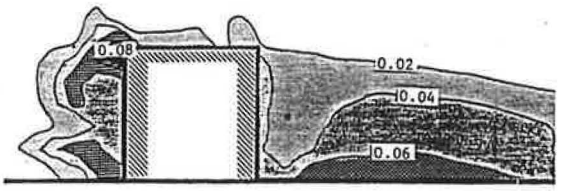

(2)solution error $\tilde{e}_h$

Fig. 5. Distribution of estimated errors for absolute velocity $(U^2+V^2+W^2)^{1/2}$. (Simulation of Case 1, non-dimensional value.) Note that non-dimensional velocity at a height of H_b is 1.0. Therefore, the maximum value of $\tilde{e}_h$ does not exceed 10% of the velocity value.

However, the maximum value of $\tilde{e}_h$ does not exceed 10% of the velocity value. From these results it becomes clear that the mesh resolution around the windward corner of the model is one of the most important factors in the prediction of the flow field with small errors.

(2) Mesh resolution around the windward corner of the model. Two cases of numerical simulation are conducted on the different types of mesh dividings and compared with the wind tunnel experiments. With Mesh 2, the mesh interval in the vicinity of the windward corner is set to the same value as that of Mesh 1 ($h_1 = H_b/6$). The velocity vectors around the model are compared in Fig. 6(1, 2). The entire flow pattern in the vertical section is well reproduced in the result of Case 2 (Mesh 2). However, the reverse flow near the side walls, which exists in experimental data, does not appear in the results of Case 2; the wake region estimated by numerical analysis is larger than that shown in the experiment. In addition, the numerically calculated velocity values in the wake behind the model are also larger than the experimental results.

The pressure coefficients (C_p) are compared in Fig. 7. In Case 2, the positive pressure on the windward wall is overestimated, and the negative pressures on the top and on the side walls are underestimated in comparison with the experimental data.

The results with Mesh 3 are also presented in Figs 6 and 7. With Mesh 3, the mesh distribution is concentrated near the windward corner and the mesh interval, h_1, near the windward corner is $H_b/24$. The reverse flows on the roof and near the side walls are clearly reproduced and the surface pressure distribution corresponds well to the experimental data, except on the leeward side of the model, as in the results with Mesh 3 (Case 3). However, there still exist some differences concerning the flow field

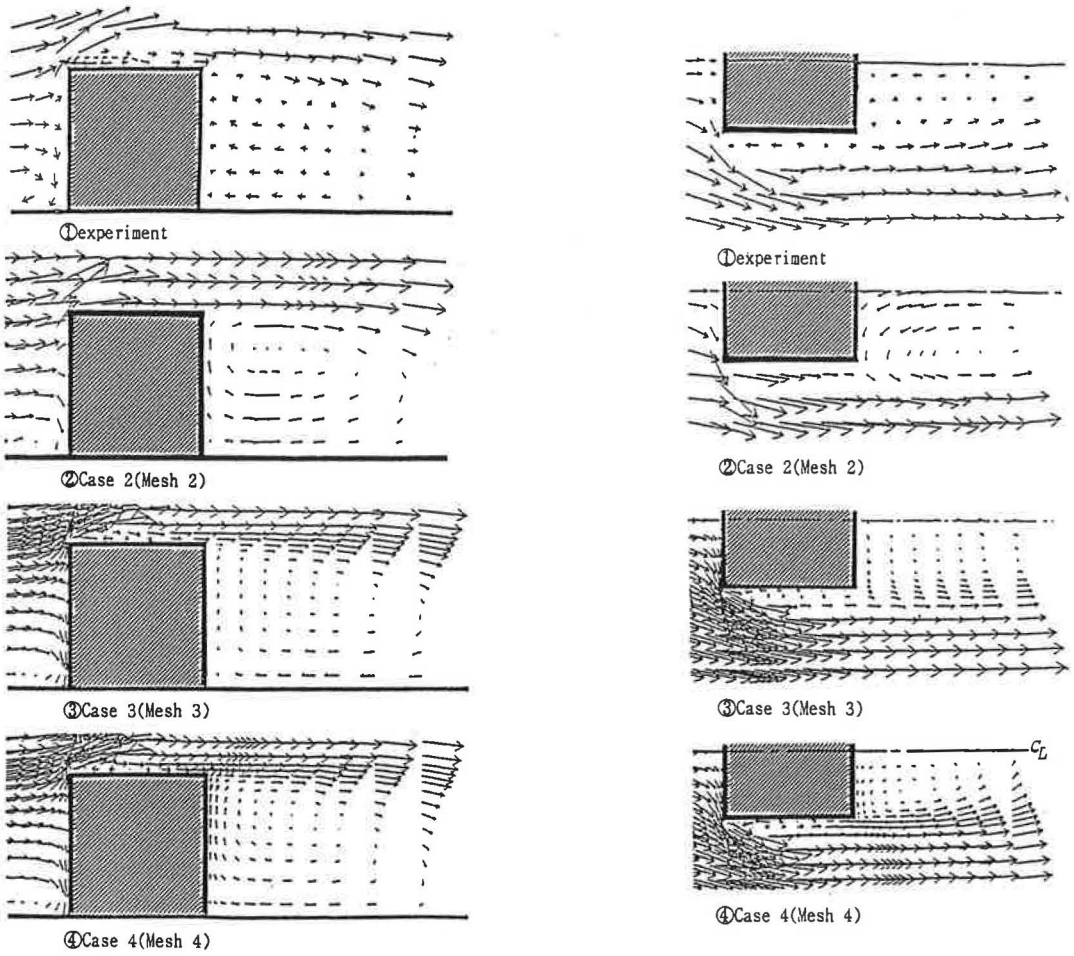

Fig. 6. Comparison of velocity vectors.

in the wake. The results with Mesh 3 (Case 3) overestimate the size of the wake and the values of the velocity of air in the wake compared with the experimental values.

Distributions of turbulent kinetic energy with Mesh 3 are compared in Fig. 8. The distribution of k is not well reproduced. The values of k in the wake are underestimated.

(3) Mesh resolution around the leeward corner. In Mesh 4, fine grid distributions are used for both the windward and the leeward side of the model. In this mesh, the interval near the windward corner is the same as that of Mesh 3, and the mesh interval near the leeward corner is a quarter of the value of that in Mesh 3 (from $H_b/6$ to $H_b/24$).

As shown in Figs 6 and 8, the correspondence of the results with Mesh 4 to the experimental data is better than those with Mesh 3. Figure 9 illustrates the production term of the transport equation for k (the production term is defined as

$$v_t S = v_t(\partial U_i/\partial x_j + \partial U_j/\partial x_i)\,\partial U_i/\partial x_j).$$

The levels of production of k in the wake become larger by decreasing the mesh interval near the leeward corner from $H_b/6$ (Case 3) to $H_b/24$ (Case 4), and the magnitudes of eddy viscosity $v_t(=C_D k^2/\varepsilon)$ increase behind the model because of the change of the production term of k as shown in Fig. 10.

Consequently, the size of the wake was predicted to be smaller, and the magnitudes of k larger in the results obtained using Mesh 4 compared to the results obtained using Mesh 3. These results imply that the mesh resolution behind the model is important in accurately predicting the flow field in the wake. The mesh resolution in Mesh 4 does not seem to be fine enough yet. It would be desirable to introduce some type of zonal mesh dividing system, such as the adaptive grid technique developed by Caruso and Ferziger [16], in order to predict the flow field in the wake precisely.

There also exists a serious difference between the distribution of k around the windward corner as predicted by the numerical results and that of the wind tunnel experiment.

2.3.2. *Influence of the boundary conditions at the solid wall (simulation of Phase 2).*

(1) Influence of length scale l in the boundary condition of Type 1. In the boundary condition of Type 1 described

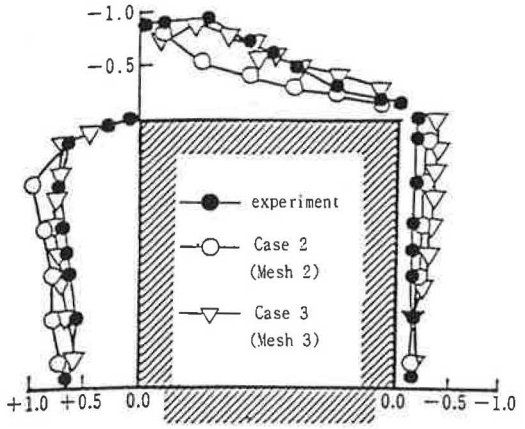

(1)vertical section at center of the model

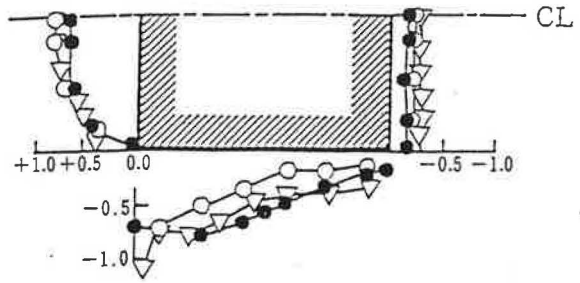

(2)horizontal section at $z=H_b/2$

Fig. 7. Comparison of surface pressure for Phase 1.

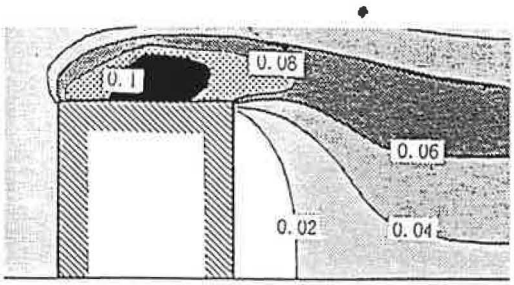

(1)experiment

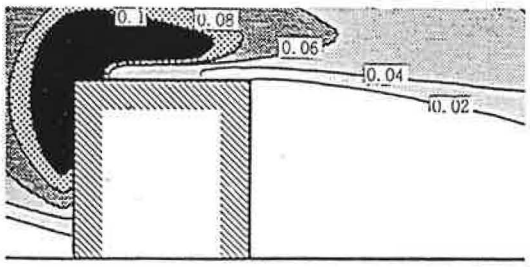

(2)Case 3(Mesh 3)

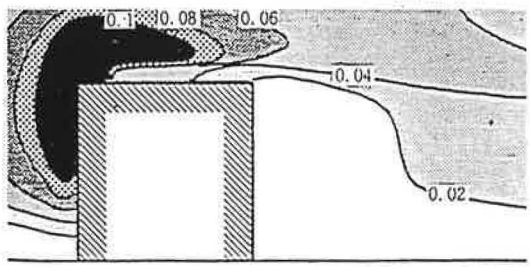

(3)Case 4(Mesh 4)

Fig. 8. Distribution of turbulent kinetic energy (k) at vertical plane (simulations of Phase 1).

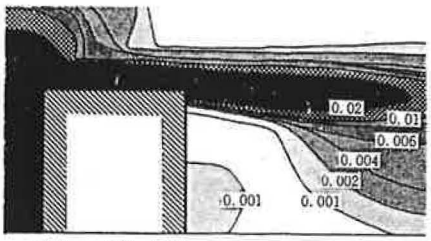

(1)Case 3(Mesh 3)

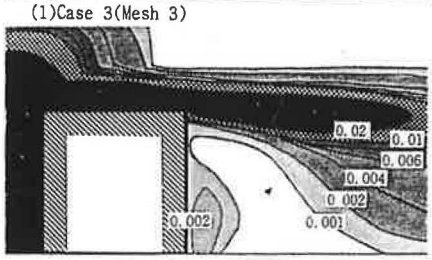

(2)Case 4(Mesh 4)

Fig. 9. Distribution of production of turbulent kinetic energy (k) at vertical plane (Phase 1).

in 2.1.4(4), the values of ε are assigned to be proportional to $k_1^{3/2}/l$, where l, defined by Equation (9), is assumed to be proportional to the mesh interval h_1. According to this formula, the value of ε is inversely proportional to the mesh interval. Thus, the value may be highly dependent upon the mesh dividings around the model. In Case 5, a coarsely divided mesh with the same resolution as that in Mesh 1 is used, but the length scale (l), which is required to assign the boundary value of ε, is set equal to the value of the fine mesh dividings (Mesh 4).

The velocity vectors on the horizontal plane are compared in Fig. 11. The reverse flow near the side walls, which does not appear in the result of Case 1, is partially reproduced in the result of Case 5 with the same coarse mesh dividings. It is found that the values of ε assigned to the solid wall have a significant influence on the predicted flow field around the model. It may also be concluded that the definition of ε used in the boundary condition of Type 1 underestimates the level of ε at the solid wall and consequently overestimates the value of ν_t. This leads to the prediction that the flow field in the vicinity of the solid wall is too diffusive, resulting in the disappearance

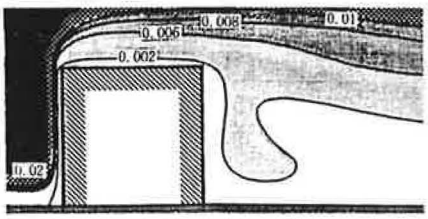

(1)Case 3(Mesh 3)

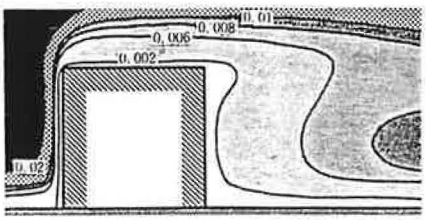

(2)Case 4(Mesh 4)

Fig. 10. Distribution of eddy viscosity ν_t at vertical plane (Phase 1).

of the reverse flow at the windward corners, although these are observed in the wind tunnel.

(2) Comparison of the boundary condition Type 1 to the boundary condition Type 2. In Case 6, the boundary conditions of Type 2 are attempted. The values of the wall unit (y^+), which should be used to assign the boundary condition Type 2, are estimated by:

$$y^+ = \tfrac{1}{2}h_1 u_*/\nu = \tfrac{1}{2}C_D^{1/4}k_1^{1/2}h_1/\nu. \quad (17)$$

Here, the initial value of k_1 is given from the result of Case 4. The estimated values of y^+ are about 230 on the windward side, 180 on the roof, 50 on the leeward side, and 60 on the side wall in the results of Case 4. Consequently, the values of ε in Type 2 at the initial conditions of Case 6, which is given by Equation (11), are nearly 3 to 4 times as large as those in Type 1 (given by Equation (9)). On the other hand, the boundary values of ε, assigned in Type 2 are not so sensitive to the mesh interval adjacent to the solid wall as those in Type 1, because the averaged value over the control volume for ε is assigned in the boundary condition of Type 2.

In the results of Case 6 (Type 2), the values of the velocity in the reverse flow regions on the roof and on the side faces are estimated to be larger than those of Case 4 (Type 1) and the agreement with the experimental data is improved, as shown in Figs 11 and 12. This is because of the fact that the level of ε increased due to the modification of the wall boundary condition from Type 1 to Type 2 and the magnitudes of k and ν_t became smaller than those in the results of Case 4.

Figure 13 shows the distribution of k in Case 6. There is little difference between the results of Case 6 and the results of Case 4 (*cf.* Fig. 8) except for the levels of k near the roof.

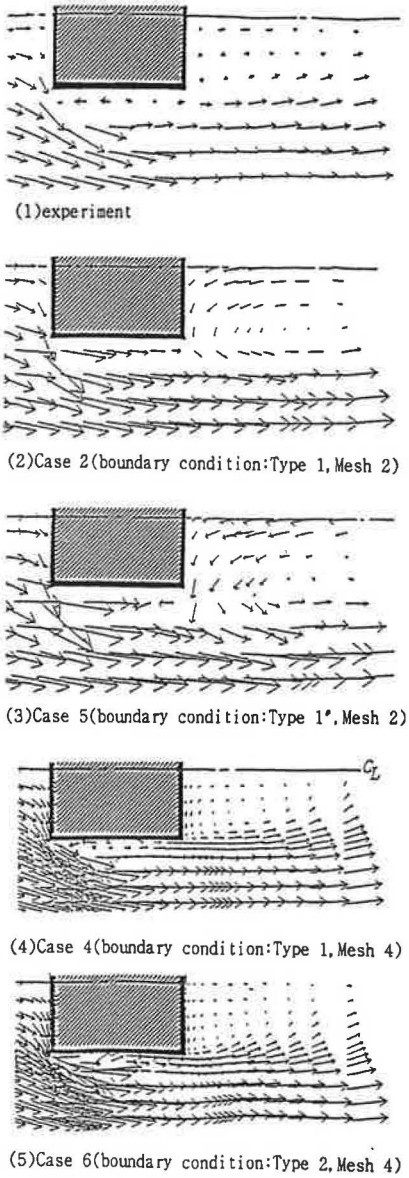

Fig. 11. Comparison of velocity vectors at horizontal plane (Phase 2, $z = H_h/2$).

3. APPLICATION OF k–ε MODEL TO THE FLOW FIELD AROUND A BUILDING COMPLEX UNDER CONSTRUCTION

3.1. *Flow around an actually planned building complex*

The results of the numerical simulation of the airflow around four buildings located on an urban renewal site in Kawasaki are presented. Figure 14 illustrates the site where four high rise buildings are situated: A is a 4 storey building, B is 19 storeys, C is 20 storeys and D is 7 storeys. The buildings are used for a shopping centre, apartments, offices and a parking garage, respectively.

Mesh dividings are shown in Fig. 15. The total number of grid points are, 52 (x-direction) × 55 (y-direction) × 42 (z-direction) = 120, 120. The computational domain covers 350 m in the x-direction, 370 m in the y-direction and 215 m in the z-direction. In the simulation, both the buildings on the site and the outer main surroundings have been reproduced as can be seen in Fig. 15.

The predicted velocity field at near ground level ($Z = 1.5$ m), with the wind direction from the SSW, is illustrated in Fig. 16. Prevailing winds in the Kawasaki district are from the SSW. The numerical results reproduced the complicated flow field at ground level. It is shown in Fig. 16 that a relatively strong wind blows into the open space between Buildings B and C. Velocity vectors at the x–x' section and the y–y' section are illustrated in Figs 17 and 18. It is well recognized in these figures that a strong wind hits the windward surface of Building C and it diverges as the gust attacks the open space surrounded by the four buildings.

The velocity vectors in the horizontal plane at $Z = 41$ m (13th floor) are shown in Fig. 19. Strong gusts occur at the windward corners of two high-rise buildings and the space between the buildings. A reverse flow at the side wall of Building C can be seen in this figure.

3.2. *Strong winds at the balconies of Building B (apartment building)*

Several cases of numerical simulations were conducted in order to investigate the characteristics of strong winds at the balconies of Building B and the shelter effects

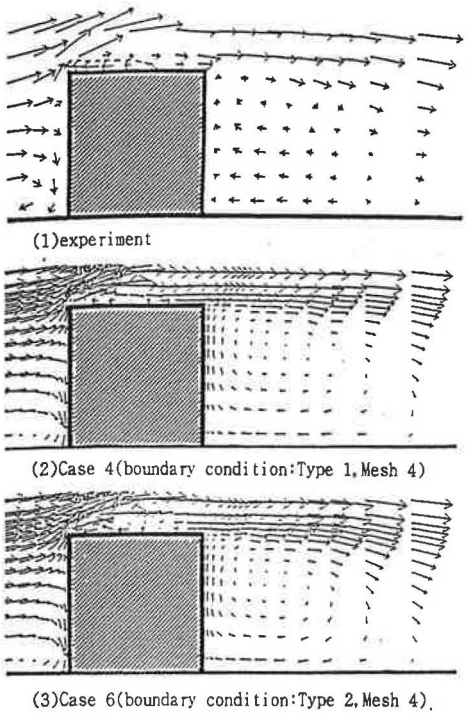

Fig. 12. Comparison of velocity vectors at vertical planes (Phase 2).

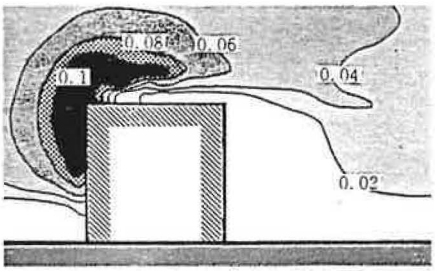

Fig. 13. Distribution of turbulent kinetic energy (k) at vertical plane (simulation of Case 6).

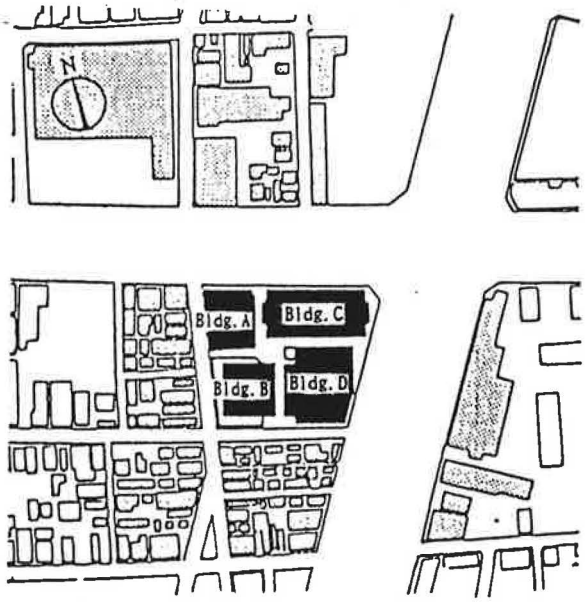

Fig. 14. Building complex under construction and its surroundings (Kawasaki, Japan).

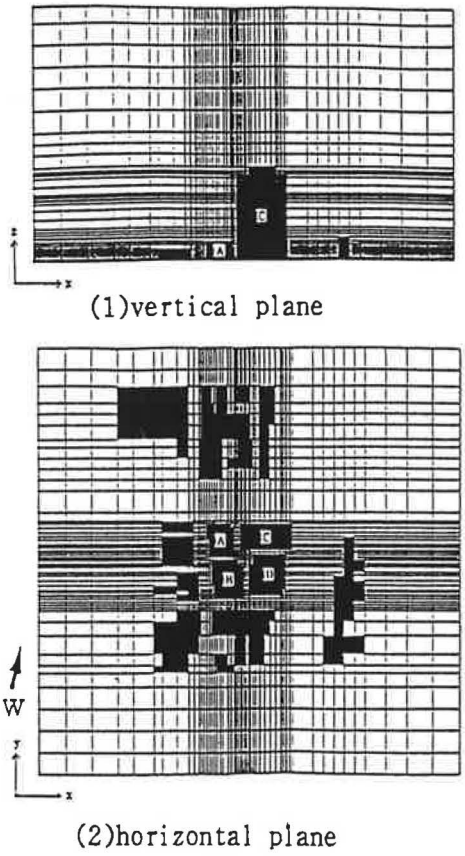

Fig. 15. Mesh dividings (Region 1).

provided by the installation of a solid fence. Figure 20 shows details of a balcony. The flow field near the windward corner of Building B at the 13th floor (Region 2, shaded area in Fig. 19) is predicted using mesh dividings, shown in Fig. 21, which are much finer than those of Region 1. In these simulations, the boundary conditions of the computational domain of Region 2 were interpolated from the results using a coarse mesh dividing of Region 1, which has a much larger computational domain.

Velocity vectors around the corner are illustrated in Figs 22 and 23. The distribution of scalar velocity $(U^2+V^2+W^2)^{1/2}$ is shown in Figs 24 and 25. The values in these figures indicate the velocity ratio to the wind velocity at a building height. It is clear that strong winds occur at the windward corner of the balcony and that the solid fence, installed at the corner, is very useful as a windbreak.

4. CONCLUSIONS

Three-dimensional numerical simulation of airflow around a cubic model and building complex under construction using the k–ε two equation turbulence model was carried out in the study. Several cases of numerical simulations were conducted in order to examine the influence of mesh resolution and boundary conditions at the solid walls. The main results of this study are summarized as follows.

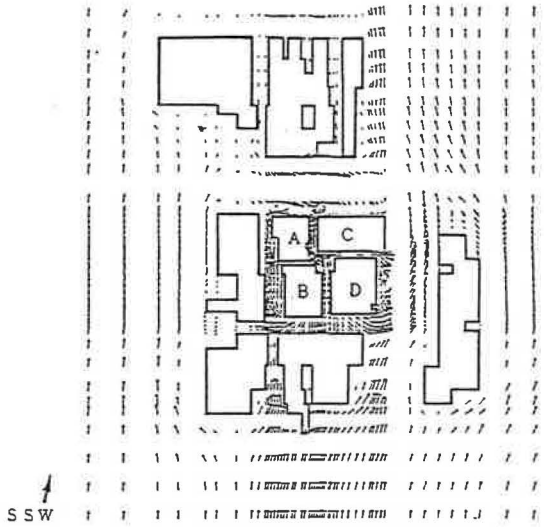

(1)flowfield around building complex and surroundings

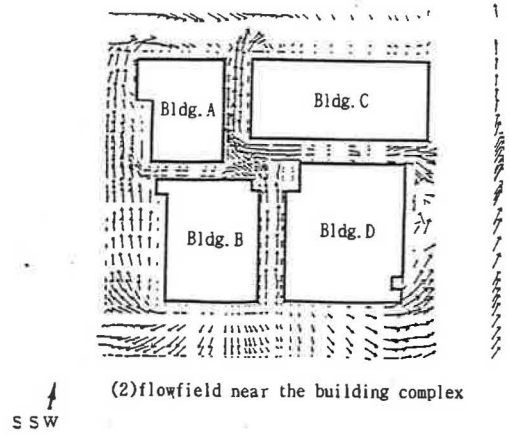

(2)flowfield near the building complex

Fig. 16. Velocity vectors at ground level ($z = 1.5$ m).

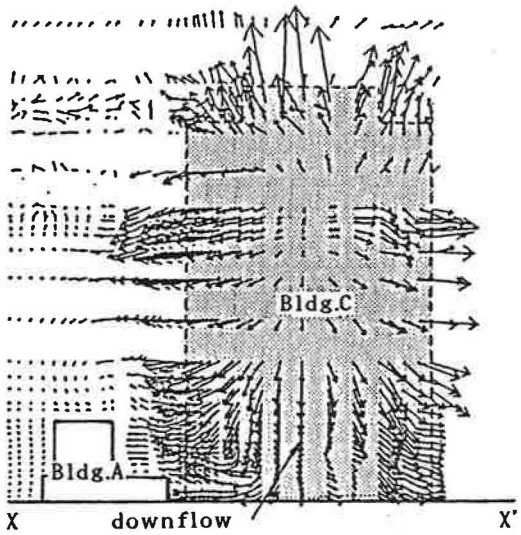

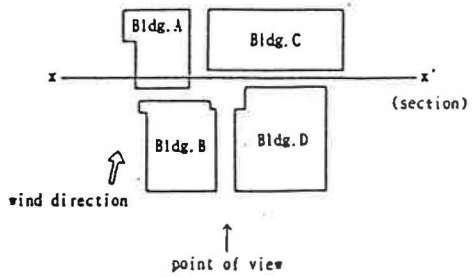

Fig. 17. Velocity vectors (vertical plane at x–x').

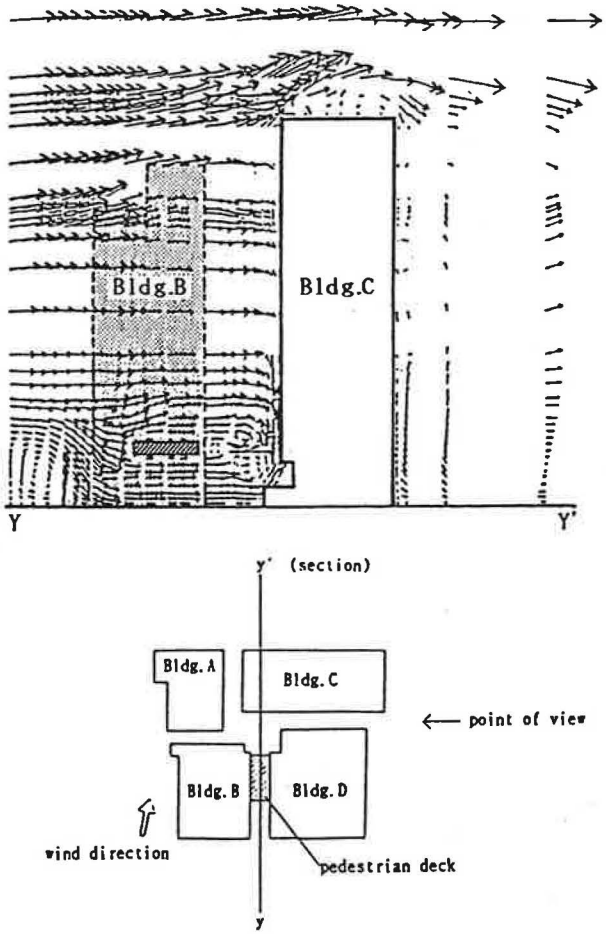

Fig. 18. Velocity vectors (vertical plane at y–y').

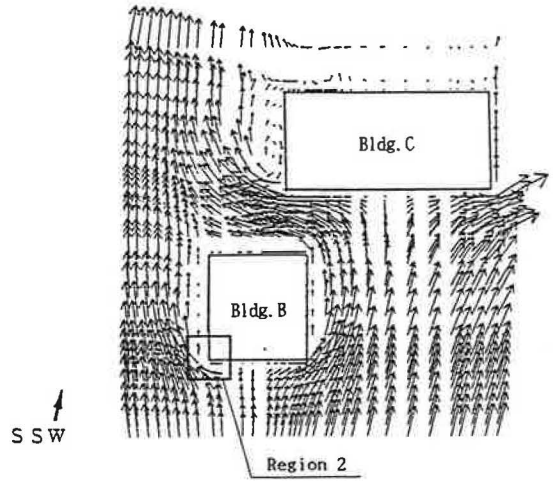

Fig. 19. Flowfield at the height of 13th floor of buildings. The shaded square area at the corner of Building B indicates the Region 2 for the next stage simulations.

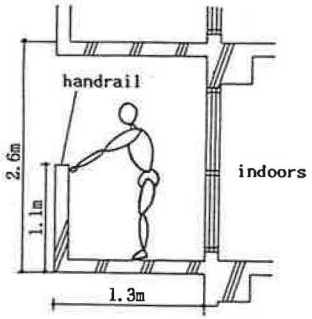

Fig. 20. Detailed view of balcony.

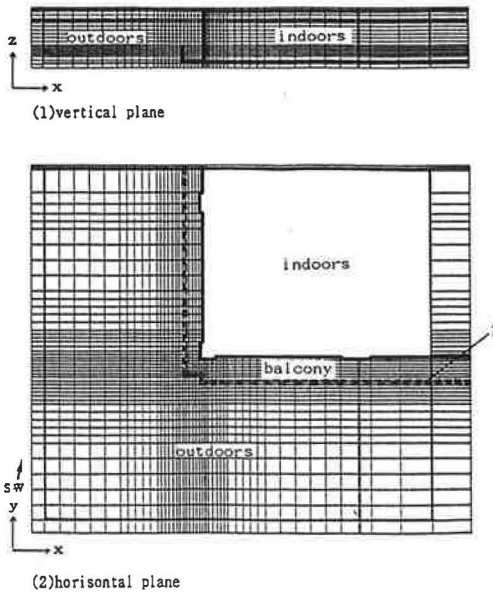

Fig. 21. Mesh dividings (Region 2).

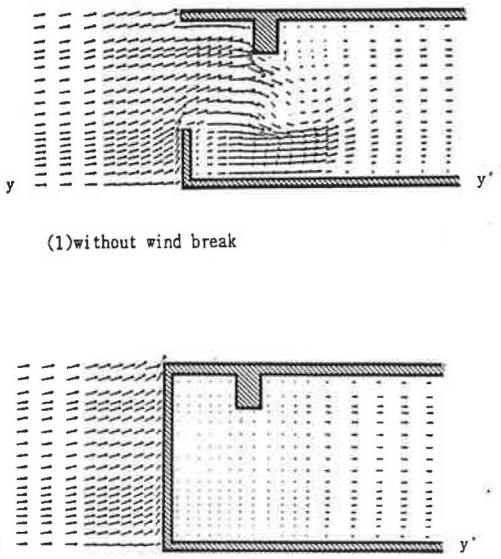

Fig. 23. Same as Fig. 22, but vertical plane at y–y'.

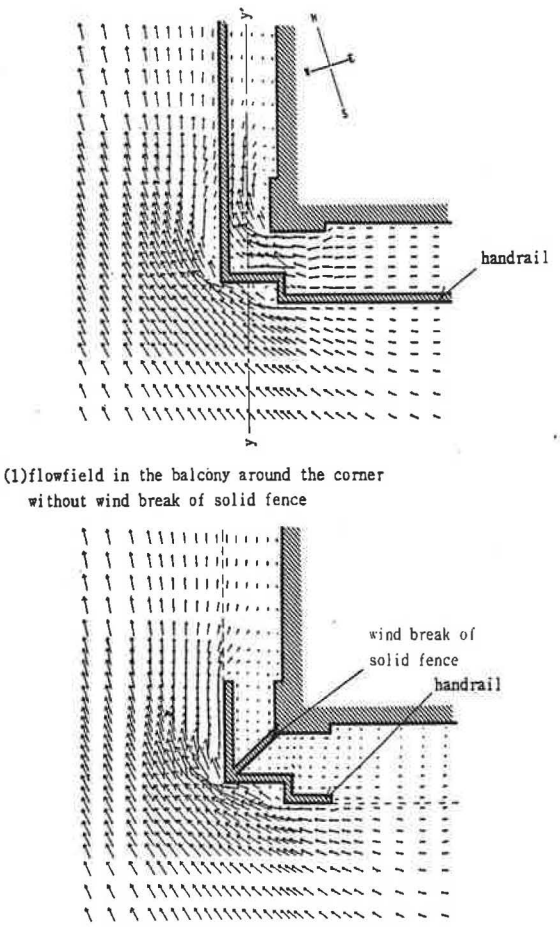

Fig. 22. Effect of wind break on strong wind at corner of balcony (horizontal plane, $z = 50$ cm).

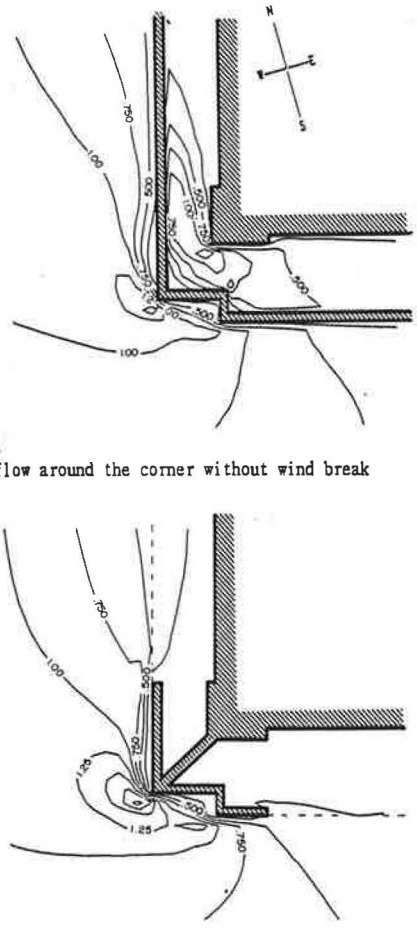

Fig. 24. Comparison of absolute velocity $(U^2+V^2+W^2)^{1/2}$ at corner of balcony (horizontal plane, $z = 50$ cm).

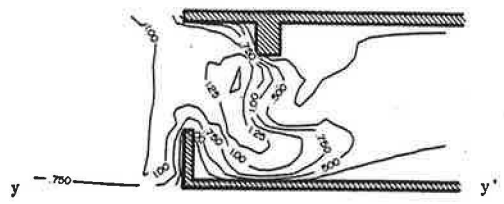

(1)without wind break

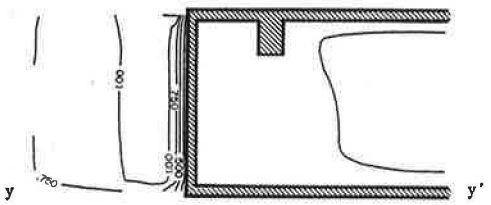

(2)with wind break

Fig. 25. Same as Fig. 24, but vertical plane at y–y'.

(1) The estimated truncation error of the velocity field centres around the windward corner when relatively coarse mesh dividings ($h = H_b/6$) are used. It is indispensable to set the mesh dividings fine enough around the windward corner in order to obtain a solution with minimal error.

(2) For the results with finer mesh dividings in which the mesh interval around the windward corner is $H_b/24$, the reverse flow on the roof and near the side walls is clearly reproduced and the distribution of the surface pressure corresponds well with the experimental results.

(3) The mesh resolution behind the model has a relatively large influence on the flow field in the wake. The levels of turbulent energy (k) and eddy viscosity (ν_t) are underestimated if the mesh resolution behind the model is not fine enough to estimate the production of k precisely.

(4) The boundary condition for ε at the solid wall has a significantly large influence on the flow field in the separation above the roof and also on the flow near the side walls at windward corners.

(5) The numerical simulation of the k–ε two equation turbulence model with fine mesh dividings can reproduce the mean velocity field and the mean pressure field around the model accurately; but there exist significant differences in the distribution of the turbulent energy (k) around the windward corner and in the wake. Further efforts should be made to improve the accuracy of the numerical simulation in the k–ε two equation turbulence model.

(6) It is also shown in this paper that numerical simulation is a powerful method for analysing the flow field in the complicated area around the building complex actually being planned.

(7) The technique of numerical simulation should be a very useful tool for the wind engineering design.

Acknowledgments—The authors would like to express their gratitude to Prof. J. H. Ferziger of Stanford University and Prof. B. E. Launder of University of Manchester, formal visiting professors at the Institute of Industrial Science, University of Tokyo, for their advice during this work.

REFERENCES

1. C. W. Hirt and J. L. Cook, Calculating three-dimensional flows around structures and over rough terrain. *J. Comput. Phys.* **10**, 324–340 (1972).
2. P. K. Yeung and S. C. Kot, Computation of turbulent flows past arbitrary two-dimensional surface-mounted obstructions. *J. Wind Engng Ind. Aerodyn.* **18**, 117–190 (1985).
3. D. A. Paterson and C. J. Alpelt, Computation of wind flows over three-dimensional buildings. *J. Wind Engng Ind. Aerodyn.* **24**, 192–213 (1986).
4. T. Hanson, D. M. Summers and C. B. Wilson, Validation of a computer simulation of wind flow over a building model. *Bldg Envir.* **21**, 97–111 (1986).
5. E. H. Mathews, Prediction of the wind-generated pressure distribution around buildings. *J. Wind Engng Ind. Aerodyn.* **25**, 219–228 (1987).
6. S. Murakami, A. Mochida and K. Hibi, Three-dimensional numerical simulation of airflow around a cubic model by means of large eddy simulation. *J. Wind Engng Ind. Aerodyn.* **25**, 291–305 (1987).
7. F. Baetke, H. Werner and H. Wengle, Computation of turbulent flow around a cube on a vector computer. Proceedings of the 6th Symposium on Turbulent Shear Flows, Vol. 9 (1987).
8. T. Tamura, K. Kuwahara and S. Shirayama, Numerical study of unsteady flow patterns and pressure distributions on a rectangular cylinder. Proceedings of the 7th International Conference on Wind Engineering, Vol. 2, pp. 41–50 (1987).
9. S. Murakami, A. Mochida and K. Hibi, Numerical prediction of velocity and pressure field around building models. Proceedings of the 7th International Conference on Wind Engineering, Vol. 2, pp. 31–40 (1987).
10. E. H. Mathews and J. P. Meyer, Computation of wind loads on a semicircular greenhouse. Proceedings of the 7th International Conference on Wind Engineering, Vol. 4, pp. 81–89 (1987).
11. B. E. Launder and D. B. Spalding, *Mathematical Models of Turbulence*. Academic Press, New York (1972).
12. F. H. Harlow and J. E. Welch, Numerical calculation of time-dependent viscous incompressible flow of fluid with free surface. *Phys. Fluids* **8**, 2182–2189 (1965).
13. B. P. Leonard, A stable and accurate convective modeling procedure based on quadratic upstream interpolation, *Comput. Methods Appl. Mech. Engng* **19**, 59–98 (1979).

14. J. A. Viecelli, A computing method for incompressible flows bounded by moving walls. *J. Comput. Phys.* **8**, 119–143 (1971).
15. B. E. Launder and D. B. Spalding, The numerical computation of turbulent flows, *Comput. Methods Appl. Mech. Engng* **3**, 269–289 (1974).
16. S. C. Caruso, J. H. Ferziger and J. Oliger, Adaptive grid techniques for elliptic fluid-flow problems. AIAA 24th Aerospace Sciences Meeting (1986).